Moving least-squares in finite strain analysis with tetrahedra support

P. Areias [a,b,*], L. Fernandes [a], R. Melicio [b,c]

[a] *DEM - Departamento de Engenharia Mecânica, Instituto Superior Técnico, Universidade de Lisboa, Avenida Rovisco Pais, 1049-001 Lisboa, Portugal* [1]
[b] *IDMEC - Instituto Superior Técnico, Universidade de Lisboa, Portugal*
[c] *INEGI - Faculdade de Engenharia, Universidade do Porto, Portugal*

ARTICLE INFO

ABSTRACT

A finite strain finite element (FE)-based approach to element-free Galerkin (EFG) discretization is introduced, based on a number of simplifications and specialized techniques in the context of a Lagrangian kernel. In terms of discretization, a quadratic polynomial basis is used, support is determined from the number of pre-assigned nodes for each quadrature point and quadrature points coincide with the centroids of tetrahedra. Diffuse derivatives are adopted, which allow for the use of convenient non-differentiable weight functions which approximate the Dirac-Delta distribution. Due to the use of a Lagrangian kernel, recent finite strain elasto-plastic constitutive developments based on the Mandel stress are adopted in a direct form. These recent developments are especially convenient from the implementation perspective, as EFG formulations for finite strain plasticity have been limited by the previous requirement of updating the kernel. We also note that, although tetrahedra are only adopted for integration in the undeformed configuration, mesh deformation is of no consequence for the results. Four 3D benchmark tests are successfully solved.

1. Introduction

Industrial-worth simulations of engineering materials processing technology are highly dependent on the quality of elasto-plastic analyses. Yield functions depend on stress values and these are, in traditional FE methods, discontinuous between elements. Compared with displacements, errors in stresses are a magnitude higher, even without accounting for constitutive constraints such as incompressibility. High order (quadratic and cubic) finite elements are typically not adopted in finite strain elasto-plastic analysis due to well-known shortcomings:

- Mesh distortion in high order elements adversely impacts convergence rate [1]. Adaptive remeshing is required more often with high-order elements. Even with a total-Lagrangian formulation, mesh distortion requires changes to the finite element mesh, since the spatial Jacobian is required to calculate the deformation gradient.
- High-order problems require dedicated techniques or architecture-intensive isogeometric formulations [2].
- Although stress quality improves with the order of the complete polynomial, in finite element methods, stresses are still discontinuous at inter-element boundaries [3]. Plasticity results are

dependent on the quality of the stresses, which is compromised even in high-order finite elements.
- Contact algorithms are often more intricate for higher-order elements. Classical meshless methods based on non-singular weight functions also involve some intricacies.

Element-free Galerkin (EFG) methods introduced by Belytschko and co-workers [4] using the least-squares results of P. Lancaster and K. Salkauskas [5] are especially appealing in the aforementioned context, as continuity of derivatives is ensured as long as weight functions are differentiable. Most EFG shortcomings have established remedies, and in this work we address the issue of the Lagrangian kernel for finite strain plasticity. Note that Rabczuk, Belytschko and Xiao [6] proved that a Lagrangian kernel is required for stability, [2] but classical finite-strain plasticity algorithms (e.g. [7,8]) combined with EFG typically update the configuration [9]. A comprehensive presentation of developments in meshless methods (including EFG) was recently published by J.-S. Chen and co-workers [10]. A related development combining partition-of-unity and least-squares is described in Cai, Zhuang and Augarde [11]. Several remedies are described, in particular for boundary conditions. Therefore, meshless methods, in particular with quadratic

---

basis and satisfying the Kronecker-Delta condition, seemingly fit these applications, as

- Since no isoparametric mapping is used, mesh distortion sensitivity is attenuated with respect to finite elements.
- Stresses are in general continuous, as long as all terms participating in the shape functions are differentiable.
- Contact algorithms are relatively simplified.
- Strain localization problems can be directly addressed via strain-gradient methods.

Several applications have been published with meshless discretization for finite strain plasticity [9], but not at the same scale of finite elements. One of the reasons might be computational cost, as more nodes are often required for the same polynomial degree, the stiffness matrix is denser. In addition, the reputation for difficult-to-impose boundary conditions still inflicts EFG, although many meshless options exist to solve this problem. Recent developments in interpolation have resurrected interest in the question of the Kronecker-Delta property, see [12].

There is also another aspect which is seldom discussed. Although Lagrangian kernels are known to be much more cost-effective than Eulerian kernels, meshless finite-strain plasticity problems are traditionally established in the deformed configuration [9], due to physical requirements. The Cauchy or Kirchhoff stress tensors are typically the best choice for the yield functions, and it is an Eulerian tensor. In the small strain side of plasticity, several successful results were published, see, e.g. [13].

In contrast, hyperelastic implementations of EFG are common, and recent papers report realistic results with high degree of continuity, see [14].

However, a newly developed fully anisotropic elasto-plastic framework based on the iteration for $\boldsymbol{C}_e$ [15] does not require the explicit form of the deformation gradient. This motivates a revisiting of the moving least-squares/EFG approach.

Since, unlike finite element formulations for finite strains, no transformation of coordinates is adopted, there is no need for a deformed-configuration Jacobian matrix. Note that in standard finite element analysis, the deformation gradient $\boldsymbol{F}$ is determined by the chain rule $\boldsymbol{F} = \boldsymbol{j} \cdot \boldsymbol{J}^{-1}$ where $\boldsymbol{j}$ is the deformed-configuration Jacobian matrix and $\boldsymbol{J}$ is the undeformed-configuration (or Lagrangian) Jacobian matrix [16]. This means that even if $\det \boldsymbol{J} > 0$, if $\det \boldsymbol{j} \leq 0$, a new mesh is required to continue the analysis.

Another effect that is often reported in the context of EFG is the volumetric locking in quasi-incompressible applications, [9,17].

In terms of discretization, technical options in this paper are the following:

- *Ab-initio* definition of the shape functions and derivatives for the entire analysis.
- Quasi-singular weight functions (see [5,18,19])
- Tetrahedra integration with single point quadrature.
- Lagrangian diffuse derivatives are adopted.
- Constitutive integration making use of the Mandel stress tensor and iteration on $\boldsymbol{C}_e$ [15].

This paper is organized as follows: Section 2 presents the interpolation, based on moving least-squares and diffuse derivatives, as well as the algorithm to guarantee a sufficiently small support radius. Section 3 presents the discretization based on the total Lagrangian approach, followed by Section 4 where the constitutive integration, fitting the developments of Section 3, is described in detail. In Section 5 four benchmark tests are performed and finally conclusions are drawn in Section 6.

2. Interpolation

2.1. General approach for moving least-squares

Interpolation with a polynomial basis and least-squares fitting was introduced by P. Lancaster and K. Salkauskas [5]. Herein, classical derivations are followed, see [4,18,20]. We introduce m as the number of terms in the polynomial basis, n as the number of supporting nodes and D as the dilation parameter, or support radius. For a given node K, distance to a given point with coordinates $\boldsymbol{X}$ is introduced with the notation $s_K(\boldsymbol{X})$. Let us consider a q−tuple of non-negative integers $\boldsymbol{\alpha} = (\alpha_1, \dots, \alpha_q) \in \mathbb{N}_0^q$. We write the absolute value as the sum: $|\boldsymbol{\alpha}| = \sum_{i=1}^q \alpha_i$. We consider the set of all polynomials of degree equal or less than p as:

$$\mathscr{P}_p = \left\{ p_{\boldsymbol{\alpha}}(\boldsymbol{X}) = X_1^{\alpha_1} \cdots X_q^{\alpha_q} \mid |\boldsymbol{\alpha}| \leq p \right\} \tag{1}$$

We now introduce a polynomial basis as an array of elements of $\mathscr{P}_p$:

$$\boldsymbol{q}(\boldsymbol{X}) = \{ p_1(\boldsymbol{X}), p_2(\boldsymbol{X}), \dots, p_m(\boldsymbol{X}) \} \quad p_i \in \mathscr{P}_p \tag{2}$$

with $\#\boldsymbol{q}(\boldsymbol{X}) = {}^{(p+q)!}/{}_{p!q!} = m$. We therefore use m elements of $\mathscr{P}$ for the polynomial basis.

The direct form (2) is known to produce conditioning difficulties. Therefore, we adopt a normalized and shifted form using a complete basis:

$$\boldsymbol{p}(\boldsymbol{X}) = \left\{ 1, \frac{\left(X_1 - \overline{X}_1\right)}{D}, \frac{\left(X_2 - \overline{X}_2\right)}{D}, \frac{\left(X_3 - \overline{X}_3\right)}{D}, \right.$$

$$\frac{\left(X_1 - \overline{X}_1\right)\left(X_2 - \overline{X}_2\right)}{D^2}, \frac{\left(X_1 - \overline{X}_1\right)\left(X_3 - \overline{X}_3\right)}{D^2},$$

$$\frac{\left(X_2 - \overline{X}_2\right)\left(X_3 - \overline{X}_3\right)}{D^2},$$

$$\left. \frac{\left(X_1 - \overline{X}_1\right)^2}{D^2}, \frac{\left(X_2 - \overline{X}_2\right)^2}{D^2}, \frac{\left(X_3 - \overline{X}_3\right)^2}{D^2}, \dots \right\} \tag{3}$$

We use $\overline{\boldsymbol{X}}$ as a centroid of the nodes within the D−radius of $\boldsymbol{X}$. Given a point with coordinates $\boldsymbol{X}$, the approximation weight of another point with coordinates $\boldsymbol{X}_I$ depends on the distance between the points $s_I(\boldsymbol{X}) = \|\boldsymbol{X} - \boldsymbol{X}_I\|$. The notation $w[s_I(\boldsymbol{X})]$ is introduced to represent this weight function of $\boldsymbol{X}$. From this basis, a $m \times n$ $\boldsymbol{P}$ Vandermonde matrix is defined by its elements as follows[3]:

$$P_{iJ} = p_i(\boldsymbol{X}_J) \quad i = 1, \dots, m, \qquad J = 1, \dots, n \tag{4}$$

The components of weight matrix, which is a function of the supporting points and the coordinates $\boldsymbol{x}$, are given by:

$$W_{IJ}(\boldsymbol{X}) = \delta_{IJ} w[s_I(\boldsymbol{X})] \qquad I, J = 1, \dots, n \tag{5}$$

A classical form of $s_I(\boldsymbol{X})$, as previously stated,

$$s_I(\boldsymbol{X}) = \|\boldsymbol{X} - \boldsymbol{X}_I\| \tag{6}$$

Applying the traditional least-squares arguments leads to the following format for the n-dimensional shape function array $\boldsymbol{N}(\boldsymbol{X})$:

$$\boldsymbol{N}(\boldsymbol{X}) = \boldsymbol{p}(\boldsymbol{X}) \cdot \boldsymbol{A}^{-1}(\boldsymbol{X}) \cdot \boldsymbol{B}(\boldsymbol{X}) \tag{7}$$

where $\boldsymbol{A}(\boldsymbol{X})$ is the $m \times m$ moment matrix $\boldsymbol{A}(\boldsymbol{X}) = \boldsymbol{B}(\boldsymbol{X}) \cdot \boldsymbol{P}^T$ and $\boldsymbol{B}(\boldsymbol{X})$ is the $m \times n$ linear combination matrix $\boldsymbol{B}(\boldsymbol{X}) = \boldsymbol{P} \cdot \boldsymbol{W}(\boldsymbol{X})$

We make use of the $\boldsymbol{Q} \cdot \boldsymbol{R}$ decomposition of $\sqrt{\boldsymbol{W}(\boldsymbol{X})} \cdot \boldsymbol{P}^T$:

$$\sqrt{\boldsymbol{W}(\boldsymbol{X})} \cdot \boldsymbol{P}^T = \boldsymbol{Q}(\boldsymbol{X}) \cdot \boldsymbol{R}(\boldsymbol{X}) \tag{8}$$

---

[3] We use uppercase indices for nodal values to facilitate the interpretation of the formulas and distinguish between polynomial terms and nodes

where $\boldsymbol{Q}(\boldsymbol{X})$ is an orthogonal matrix and $\boldsymbol{R}(\boldsymbol{X})$ is an upper triangular matrix [21]. A classical Gram–Schmidt algorithm for the $\boldsymbol{Q} \cdot \boldsymbol{R}$ decomposition is used. For our application, only $\boldsymbol{R}(\boldsymbol{X})$ is required. It is straightforward to obtain, from (7), the following:

$$\boldsymbol{N}(\boldsymbol{X}) = p(\boldsymbol{X}) \cdot \boldsymbol{R}^{-1}(\boldsymbol{X}) \cdot \boldsymbol{R}^{-T}(\boldsymbol{X}) \cdot \boldsymbol{B}(\boldsymbol{X}) \tag{9}$$

Therefore, this operation is relatively inexpensive since it consists of two triangular solves. Omitting the dependence on $\boldsymbol{X}$, we have

$$\boldsymbol{R}^T \cdot \boldsymbol{U}_1 = \boldsymbol{B} \tag{10}$$

$$\boldsymbol{R} \cdot \boldsymbol{U}_2 = \boldsymbol{U}_1 \tag{11}$$

where $\boldsymbol{U}_2$ is a $m \times n$ matrix, which suffices to define the shape functions. Reintroducing the dependence on $\boldsymbol{X}$, the result is:

$$\boxed{\boldsymbol{N}(\boldsymbol{X}) = \boldsymbol{p}(\boldsymbol{X}) \cdot \boldsymbol{U}_2(\boldsymbol{X})} \tag{12}$$

The interpolated value $\phi(\boldsymbol{X})$ is obtained by linear combination of nodal values $\boldsymbol{\phi} = \{\phi_1, \phi_2, \dots, \phi_n\}$ $\phi(\boldsymbol{X}) = \boldsymbol{N}(\boldsymbol{X}) \cdot \boldsymbol{\phi}$. In terms of components, Eq. (7) is written as:

$$N_L(\boldsymbol{X}) = p_j(\boldsymbol{X}) U_{2jL}(\boldsymbol{X}) \qquad L = 1, \dots, n; \quad j, k = 1, \dots, m \tag{13}$$

First derivative of $N_L(\boldsymbol{x})$ with respect to coordinates x_m, $m = 1, 2, 3$ is here denoted as:

$$\begin{aligned} N'_L(\boldsymbol{X}) =& p'_j(\boldsymbol{X}) U_{2jL}(\boldsymbol{X}) \\ & - p_j(\boldsymbol{X}) A_{jl}^{-1}(\boldsymbol{X}) A'_{lp}(\boldsymbol{X}) U_{2pL}(\boldsymbol{X}) \\ & + p_j(\boldsymbol{X}) A_{jk}^{-1}(\boldsymbol{X}) B'_{kL}(\boldsymbol{X}) \end{aligned} \tag{14}$$

where

$$B'_{kL}(\boldsymbol{X}) = P_{kJ} W'_{JL}(\boldsymbol{X}) \tag{15}$$

$$A'_{lp}(\boldsymbol{X}) = B'_{lL}(\boldsymbol{X}) P_{pL} \tag{16}$$

In terms of $p'_j(\boldsymbol{X})$ and $W'_{JI}(\boldsymbol{X})$, Eq. (14) can be written as a sum of two terms:

$$N'_L(\boldsymbol{X}) = N^\star_L(\boldsymbol{X}) + N^\bullet_L(\boldsymbol{X}) \tag{17a}$$

where

$$N^\star_L(\boldsymbol{X}) = p'_j(\boldsymbol{X}) U_{2jL}(\boldsymbol{X}) \tag{17b}$$

and

$$N^\bullet_L(\boldsymbol{X}) = p_j(\boldsymbol{X}) A_{jl}^{-1}(\boldsymbol{X}) P_{lM} W'_{MQ}(\boldsymbol{X}) \left[\delta_{QL} - P_{pQ} U_{2pL}(\boldsymbol{X}) \right] \tag{17c}$$

It is a tradition to identify (17b) as the *diffuse* derivative. We can clearly prove that $N^\bullet_L(\boldsymbol{X}_K) = 0$ if the Kronecker-Delta condition is satisfied $N_L(\boldsymbol{X}_K) = \delta_{LK}$:

$$\begin{aligned} N_L(\boldsymbol{X}_K) &= \delta_{LK} \\ & \Rightarrow P_{jK} A_{jn}^{-1}(\boldsymbol{X}_K) B_{nL}(\boldsymbol{X}_K) = \delta_{LK} \\ & \Rightarrow N^\bullet_L(\boldsymbol{X}_K) = 0 \end{aligned}$$

2.2. Quasi-singular weight function

Singular weight functions are known to produce an interpolation satisfying the Kronecker-Delta property [5]. Quasi-singular functions have been adopted to approximate this property [18]. The following quasi-singular weight function is introduced (see, e.g. [18,19]):

$$w[s_I(\boldsymbol{X})] = \begin{cases} \left[s_I^2(\boldsymbol{X})/D^2 + \text{tol}^2 \right]^{-1} - \left[1 + \text{tol}^2 \right]^{-1} & s_I \leq D \\ 0 & s_I > D \end{cases} \tag{18}$$

where $\text{tol} \in \mathbb{R}^+$ is a tolerance parameter. The maximum value of $w[s_I]$ is obtained as:

$$w[0] = 1/(\text{tol}^2 + \text{tol}^4) \tag{19}$$

Here we adopt tol=1×10^{-3}. The Kronecker-Delta property is approximately satisfied:

$$N_I(\boldsymbol{X}_J) \cong \delta_{IJ} \tag{20}$$

Derivatives of $w[s_I]$ with respect to s_I are trivially given by

$$\frac{\mathrm{d} w[s_I]}{\mathrm{d} s_I} = - \frac{2 D^2 s_I}{\left(D^2 \text{tol}^2 + s_I^2 \right)^2} \tag{21}$$

A plot of the shape functions and derivatives for tol $= 1 \times 10^{-3}$ is exhibited in Fig. 1 for $D = 2$ (first column) and $D = 4$ (second column).

Strong versions of this weighting are available, see M Dehghan, [22], but entail a more intricate implementation.

2.3. Lumping

An implementation-oriented approach is adopted. Using the tetrahedral support, a composition of shape functions is performed. Only the undeformed Jacobian is required and hence the formulation is nearly insensitive to deformation-induced mesh distortion.

We now use the nodes to establish localized shape functions in the tetrahedra. This concept is based on the original shape-function derivatives at the nodes of each tetrahedra. Using node M, the corresponding derivative is given by:

$$N'_M(\boldsymbol{X}_M) = p'_j(\boldsymbol{X}_M) U_{2jM}(\boldsymbol{X}_M) \tag{22}$$

Rewriting the derivative, we have:

$$\boxed{\frac{\mathrm{d} N_M(\boldsymbol{X}_M)}{\mathrm{d} \boldsymbol{X}_m} = \frac{\mathrm{d} p_j(\boldsymbol{X}_M)}{\mathrm{d} \boldsymbol{X}_m} U_{2jM}(\boldsymbol{X}_M)} \tag{23}$$

Standard finite element shape functions are adopted now for interpolation of the nodal values. This is akin to the partition of unity method (PUFEM) but makes use of nodes not belonging to the integration domain (the finite element itself).

For a tetrahedron we have the following volume-based shape functions:

$$\boldsymbol{M}(\boldsymbol{\xi}) = \{ \xi_1, \xi_2, 1 - \xi_1 - \xi_2 - \xi_3, \xi_3 \} \tag{24}$$

We have $0 \leq \xi_i \leq 1$ with

$$\boldsymbol{J} = \left[\begin{array}{c|c|c} \boldsymbol{X}_1 - \boldsymbol{X}_3 & \boldsymbol{X}_2 - \boldsymbol{X}_3 & \boldsymbol{X}_4 - \boldsymbol{X}_3 \end{array} \right] \tag{25}$$

The derivatives of the shape functions $\boldsymbol{M}$ with respect to $\boldsymbol{X}$ are given as Eq. (26) in Box I:

The shape functions for a given element are given by:

$$N^\star_M(\boldsymbol{X}) = M_K(\boldsymbol{\xi}) N_M \tag{27}$$

$$M \in \text{Vis}[G(K)] \tag{28}$$

where $\text{Vis}[G(K)]$ indicates the visibility of node K. Implementation is based on the following steps, performed at the start of the analysis:

1. For each face F of the tetrahedra mesh, flag it if it's a boundary face. Each boundary face shares only one tetrahedron.
2. For each node K, flag it as boundary node if it shares a boundary face.
3. Loop over all nodes that are not at the boundary:

   (a) For each non-boundary node K determine the smallest edge containing K.
   (b) Sets r_L as 10% of its length as the maximum perturbation.
   (c) Using a sphere of radius r_L and center K randomly determines the new position of node K inside the sphere.

4. Loop over all tetrahedra. For tetrahedron E:
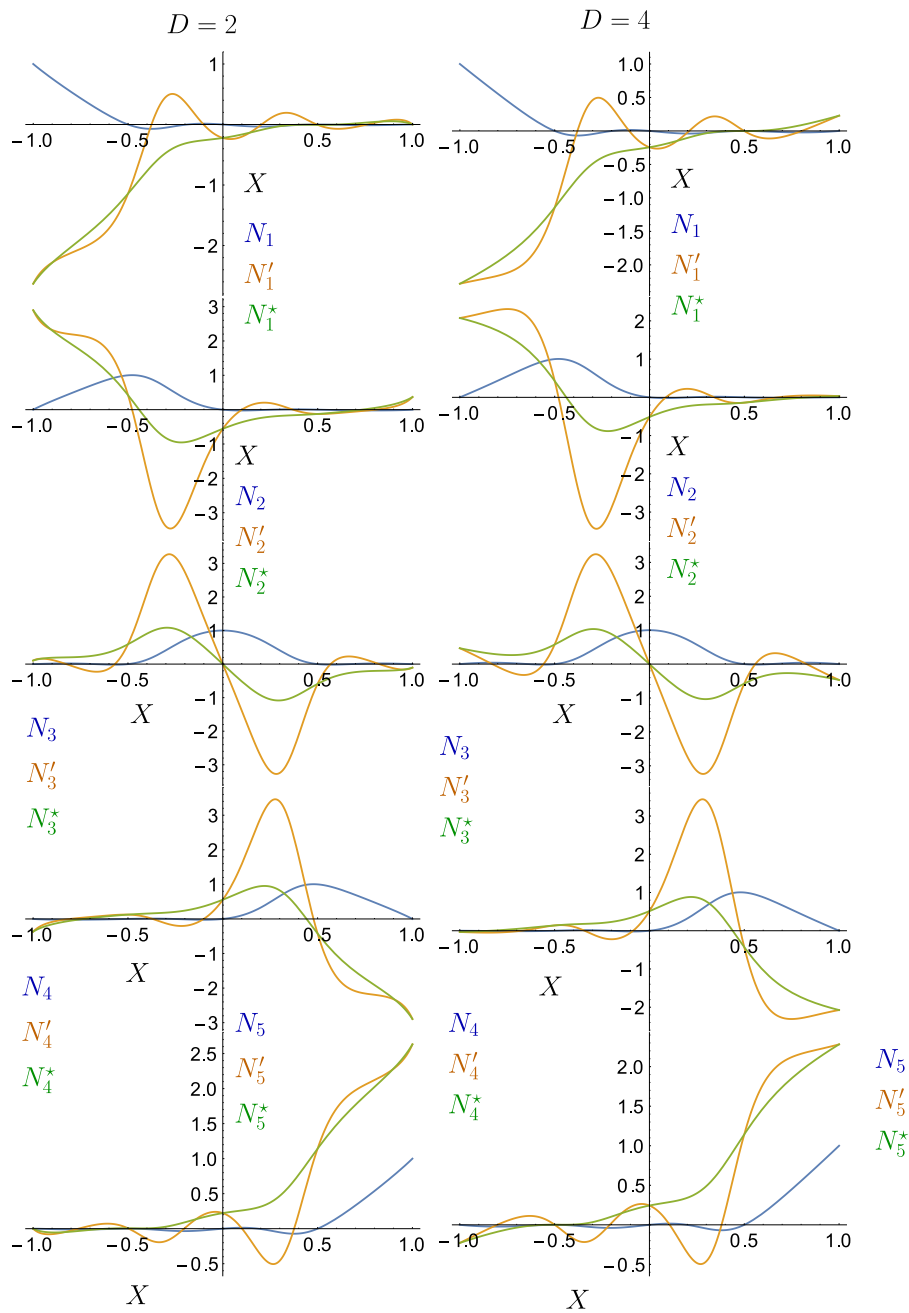
   (a) For a given list of size $n \geq 4$, insert:

Fig. 1. Shape functions, diffuse and total derivatives for a quadratic basis, $X = \{-1, -0.5, 0, +0.5, +1\}$ with $D = 2$ and $D = 4$.

$$\frac{\mathrm{d}\boldsymbol{M}}{\mathrm{d}\boldsymbol{X}} = \begin{bmatrix} \left[\boldsymbol{J}^{-1}\right]_{11} & \left[\boldsymbol{J}^{-1}\right]_{12} & \left[\boldsymbol{J}^{-1}\right]_{13} \\ \left[\boldsymbol{J}^{-1}\right]_{21} & \left[\boldsymbol{J}^{-1}\right]_{22} & \left[\boldsymbol{J}^{-1}\right]_{23} \\ -\left[\boldsymbol{J}^{-1}\right]_{11} - \left[\boldsymbol{J}^{-1}\right]_{21} - \left[\boldsymbol{J}^{-1}\right]_{31} & -\left[\boldsymbol{J}^{-1}\right]_{12} - \left[\boldsymbol{J}^{-1}\right]_{22} - \left[\boldsymbol{J}^{-1}\right]_{32} & -\left[\boldsymbol{J}^{-1}\right]_{13} - \left[\boldsymbol{J}^{-1}\right]_{23} - \left[\boldsymbol{J}^{-1}\right]_{33} \\ \left[\boldsymbol{J}^{-1}\right]_{31} & \left[\boldsymbol{J}^{-1}\right]_{32} & \left[\boldsymbol{J}^{-1}\right]_{33} \end{bmatrix} \qquad (26)$$

Box I.

i. All nodes of the tetrahedron.

ii. Other $n - 4$ closest nodes to the centroid of E.

(b) Use the farthest node in the list to determine the support radius D for tetrahedron E.

(c) Use Eqs. (23) to calculate the shape function derivatives.

5. In the Newton–Raphson iteration loop, only C is calculated, shape function derivatives are stored in memory.

3. Discretized equilibrium equations

A straightforward total-Lagrangian implementation is followed (see, e.g. [16]). We make use of the definition of the right Cauchy–Green tensor:

$$C\left(X_h\right) = F^T\left(X_h\right) \cdot F\left(X_h\right) \tag{29}$$

For a given point X_h with discrete support Ω_{X_h}, we have:

$$F\left(X_h\right) = \frac{\mathrm{d}x_h}{\mathrm{d}X_h} = \sum_{L \in \Omega_{X_h}} \left(\frac{\mathrm{d}N_L\left(X_h\right)x_L}{\mathrm{d}X_h}\right) \tag{30}$$

In terms of components and omitting the dependence on X_h, we obtain the components of F as:

$$F_{ij} = \frac{\mathrm{d}N_L}{\mathrm{d}X_j}x_{iL} \tag{31}$$

Using the variation symbol, δ we introduce the variation of F, in the equilibrium sense, as:

$$\delta F_{ij} = \frac{\mathrm{d}N_L}{\mathrm{d}X_j}\delta x_{iL} \tag{32}$$

Introducing the notation $N_{jL} = \mathrm{d}N_L/\mathrm{d}X_j$ for the shape-function derivatives, the following results for C and its first and second variations are obtained:

$$C_{ij} = N_{iK}N_{jL}x_{kK}x_{kL} \Rightarrow$$
$$\delta C_{ij} = N_{iK}N_{jL}\left(x_{kL}\delta x_{kK} + x_{kK}\delta x_{kL}\right)$$
$$\dot{C}_{ij} = N_{iK}N_{jL}\left(x_{kL}\dot{x}_{kK} + x_{kK}\dot{x}_{kL}\right)$$
$$\delta\dot{C}_{ij} = N_{iK}N_{jL}\left(\dot{x}_{kL}\delta x_{kK} + x_{kK}\delta x_{kL}\right)$$

Equilibrium is established in weak form by the use of the second Piola–Kirchhoff stress S and the spatial configuration variation δx:

$$\frac{1}{2}\int_{\Omega_0} S : \delta C \,\mathrm{d}\Omega_0 = f_{\text{ext}} \cdot \delta x \tag{33}$$

For the application of Newton–Raphson iteration, we require the first variation of (33). To avoid confusion with the variation symbol δ, we use the time-derivative to denote the variation of equilibrium. By taking this time-derivative variation, the tangent modulus $\mathscr{C}$ is employed to read:

$$\frac{1}{2}\int_{\Omega_0} S : \delta\dot{C}\mathrm{d}\Omega_0 + \frac{1}{4}\int_{\Omega_0}\delta C : \mathscr{C} : \dot{C}\,\mathrm{d}\Omega_0 = f_{\text{ext}}\cdot\delta x - \frac{1}{2}\int_{\Omega_0} S : \delta C\,\mathrm{d}\Omega_0 \tag{34}$$

where f_{ext} is the external load vector and is the nodal velocity vector. Note that, in the implementation, the second derivative of C is required in $\delta\dot{C}$. In Voigt form (see [23]), we have the following internal force and tangent stiffness:

$$f_L = \int_{\Omega_0} B_L^T \cdot \hat{S}\,\mathrm{d}\Omega_0 \tag{35}$$

$$K_{KL} = \int_{\Omega_0} B_K^T \cdot \mathscr{C} \cdot B_L\,\mathrm{d}\Omega_0 + \int_{\Omega_0} B_K^{\star T} \cdot \check{S} \cdot B_L^{\star}\,\mathrm{d}\Omega_0 \tag{36}$$

Omitting dependence on X, notation in (35)–(36) is as follows:

$$B_L = \begin{bmatrix} F_{11}N_{1L} & F_{21}N_{1L} & F_{31}N_{1L} \\ F_{12}N_{2L} & F_{22}N_{2L} & F_{32}N_{2L} \\ F_{13}N_{3L} & F_{23}N_{3L} & F_{33}N_{3L} \\ F_{11}N_{2L}+F_{12}N_{1L} & F_{21}N_{2L}+F_{22}N_{1L} & F_{31}N_{2L}+F_{32}N_{1L} \\ F_{13}N_{1L}+F_{11}N_{3L} & F_{23}N_{1L}+F_{21}N_{3L} & F_{33}N_{1L}+F_{31}N_{3L} \\ F_{12}N_{3L}+F_{13}N_{2L} & F_{22}N_{3L}+F_{23}N_{2L} & F_{32}N_{3L}+F_{33}N_{2L} \end{bmatrix} \tag{37}$$

Specific form of $B_K^{\star}$ in (36) is not needed at this point, and can be consulted in [3]. The Voigt form of the second Piola–Kirchhoff stress is given by:.

$$\hat{S} = \begin{Bmatrix} S_{11} \\ S_{22} \\ S_{33} \\ S_{12} \\ S_{13} \\ S_{23} \end{Bmatrix} \tag{38}$$

We also have:

$$B_K^{\star T} \cdot \check{S} \cdot B_L^{\star} = r_{KL}I_{3\times 3} \tag{39}$$

where

$$r_{KL} = \begin{Bmatrix} N_{1K} \\ N_{2K} \\ N_{3K} \end{Bmatrix}^T \cdot \begin{bmatrix} S_{11} & S_{12} & S_{13} \\ S_{12} & S_{22} & S_{23} \\ S_{13} & S_{23} & S_{33} \end{bmatrix} \cdot \begin{Bmatrix} N_{1L} \\ N_{2L} \\ N_{3L} \end{Bmatrix} \tag{40}$$

which is a compact form for the geometric stiffness. In contrast with advanced finite element formulations [24,25], these are classical and direct derivations. In addition, shape functions and corresponding derivatives can be calculated once, in the beginning of the solution process.

4. Hyperelasticity/plasticity using the elastic mandel stress tensor

4.1. Formulation

The Mandel stress tensor approach to finite-strain plasticity is adopted [26,27]. We make use of the Kröner–Lee decomposition [28,29] (see also [30]):

$$F = F_e \cdot F_p \tag{41}$$

Using (41), the velocity gradient is determined by its definition and then partitioned as follows:

$$L = \dot{F} \cdot F^{-1} = L_e + F_e \cdot L_p \cdot F_e^{-1} \tag{42}$$

with $L_e = \dot{F}_e \cdot F_e^{-1}$, the elastic velocity gradient and $L_p = \dot{F}_p \cdot F_p^{-1}$, the plastic velocity gradient. The second Piola–Kirchhoff stress is a function of the elastic part of F by means of $C_e = F_e^T \cdot F_e$ (cf. [31] page 166), the second Piola–Kirchhoff stress at the intermediate configuration is given by $S_e\left(C_e\right)$ (see [32]), from which energy consistency results in a second Piola–Kirchhoff stress $S = F_p^{-1} \cdot S_e\left(C_e\right) \cdot F_p^{-T}$. In the hyperelastic case, a strain–energy density function $\psi\left(C_e\right)$ exists such as

$$S_e\left(C_e\right) = 2\mathrm{d}\psi(C_e)/\mathrm{d}C_e \tag{43}$$

The Neo-Hookean model is used, with the following strain–energy density function:

$$\psi(C_e) = \frac{\mu}{2}\left[\mathrm{tr}\left(C_e\right) - 3\right] - \mu\log\sqrt{\det\left(C_e\right)} + \frac{\lambda}{2}\left[\log\sqrt{\det\left(C_e\right)}\right]^2 \tag{44}$$

The flow law follows similar arguments [27], assuming that the initial plastic deformation gradient corresponds to the identity, $\left[F_p\right]_0 = I$. Agreeing with standard derivations on plasticity, a yield function ϕ is introduced, as well as a plastic multiplier $\dot{\gamma}$. Introducing the notation $Q_p = F_p^{-1}$. We summarize the constitutive system as:

$$S = Q_p \cdot S_e\left(C_e\right) \cdot Q_p^T \tag{45}$$

$$\dot{Q}_p = -\dot{\gamma}Q_p \cdot N\left[T_e\right] \tag{46}$$

$$\left[Q_p\right]_0 = I \tag{47}$$

$$< \phi\left(T_e\right) + \dot{\gamma} > -\dot{\gamma} = 0 \tag{48}$$

with $< \bullet > = \frac{\bullet + |\bullet|}{2}$ being the unit ramp function. In (46), the Mandel stress [26] T_e is given by:
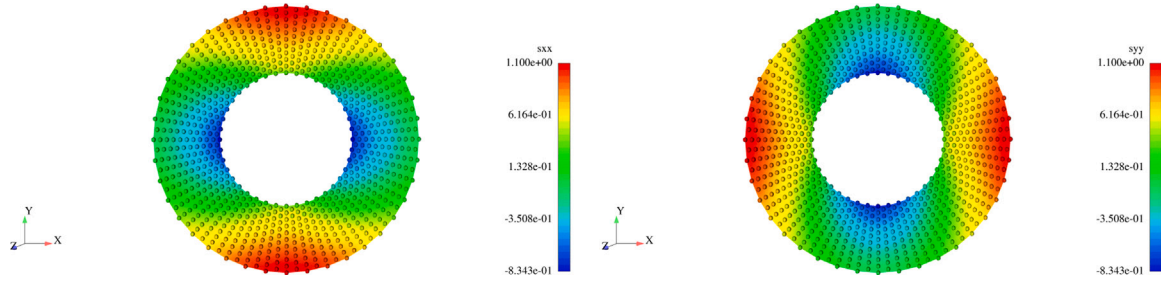
$$T_e = C_e \cdot S_e\left(C_e\right) \tag{49}$$

Fig. 2. Elasto-plastic pressurized cylinder, closed-form solutions obtained from Chapter 5 of Chakrabarty [33]. Inner radius: $a = 1$, outer radius: $b = 2$ and $\sigma_y = 1$, $p = 0.800377$.
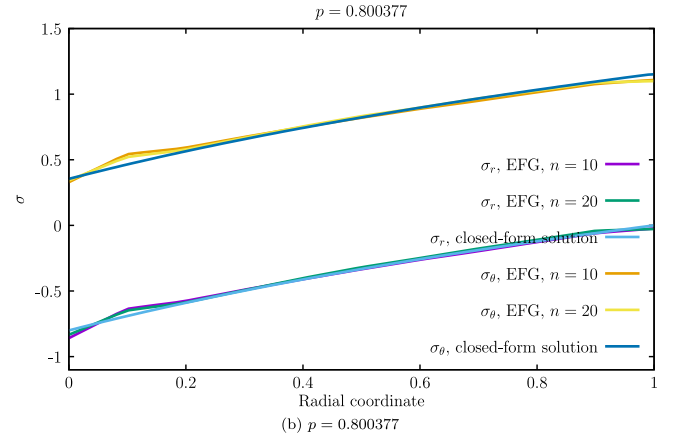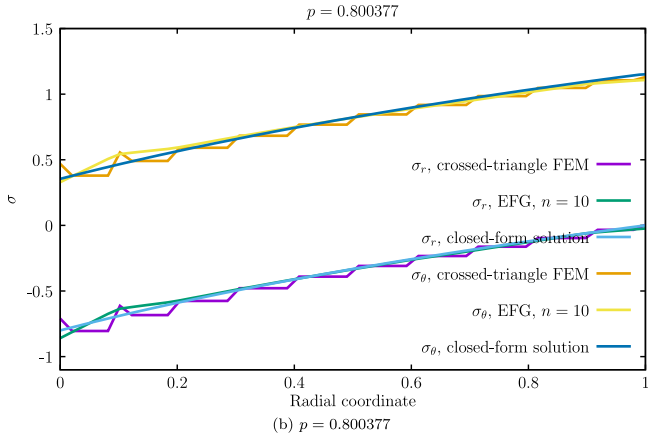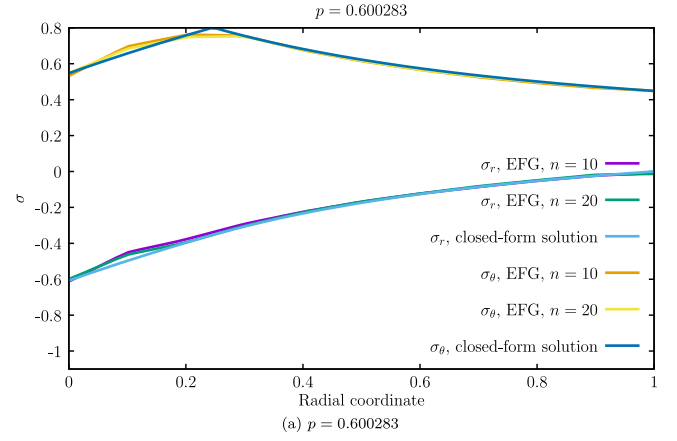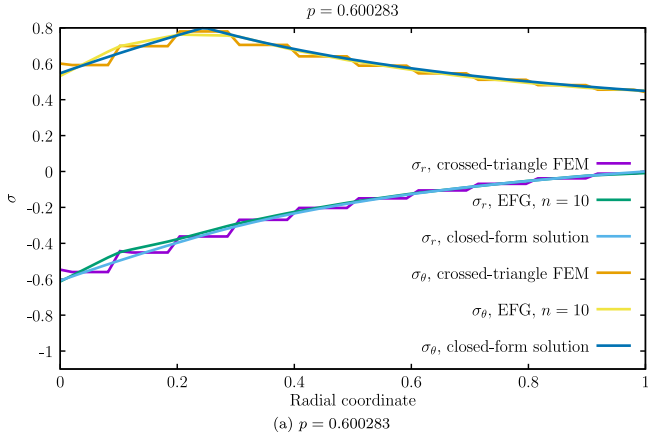

Fig. 3. Stress results for the pressurized cylinder for two values of the pressure.

Fig. 4. Comparison between $n = 10$ and $n = 20$ for the pressurized cylinder for two values of the pressure.

Assuming an associated flow law [30], we have the flow vector $\boldsymbol{N}\left(\boldsymbol{T}_e\right)$ determined from the derivative of $\phi\left(\boldsymbol{T}_e\right)$:

$$\boldsymbol{N}(\boldsymbol{T}_e) = \mathrm{d}\phi(\boldsymbol{T}_e)/\mathrm{d}\boldsymbol{T}_e \tag{50}$$

When hardening is present, power equivalence provides the effective plastic strain rate $\dot{\varepsilon}_p$ as a function of the yield stress σ_y:

$$\dot{\varepsilon}_p = \dot{\gamma}\frac{\boldsymbol{T}_e : \boldsymbol{N}(\boldsymbol{T}_e)}{\sigma_y} \tag{51}$$

4.2. Constitutive integration

For the constitutive integration, we use superscripts n and $n + 1$ to identify two consecutive time-steps and Δt as the time-step size.

Applying the backward-Euler method for $\dot{\boldsymbol{Q}}_p$ and $\dot{\gamma}$ results in:

$$\boldsymbol{Q}_p^{n+1} = \boldsymbol{Q}_p^n \cdot \underbrace{\left[\boldsymbol{I} + \Delta\gamma\,\widehat{\boldsymbol{N}}\left(\boldsymbol{C}_e^{n+1}\right)\right]^{-1}}_{\left[\Delta\widehat{\boldsymbol{Q}}\left(\boldsymbol{C}_e^{n+1},\Delta\gamma\right)\right]^{-1}} \tag{52}$$

$$\gamma^{n+1} = \gamma^n + \underbrace{\dot{\gamma}^{n+1}\,\Delta t}_{\Delta\gamma} \tag{53}$$

We now define the elastic trial Cauchy–Green tensor as $\boldsymbol{C}_e^{\star} = \left[\boldsymbol{Q}_p^n\right]^T \cdot \boldsymbol{C}^{n+1} \cdot \boldsymbol{Q}_p^n$. Introducing the function $\widehat{\boldsymbol{C}}_e^{\star}\left(\boldsymbol{C}^{n+1}\right) = \left(\boldsymbol{Q}_p^n\right)^T \cdot \boldsymbol{C}^{n+1} \cdot \boldsymbol{Q}_p^n$, the

Properties (consistent units)

Quasi-incompressible Neo-Hookean

$\kappa = 400889.806$

$\mu = 80.194$

⭘ Monitored node

$u_1 = 0, \, u_3 = 0$

$p = 3.2 \times 10^5$

$u_3 = 0$

1

$u_1 = 0$

$u_2 = 0$

Meshes:

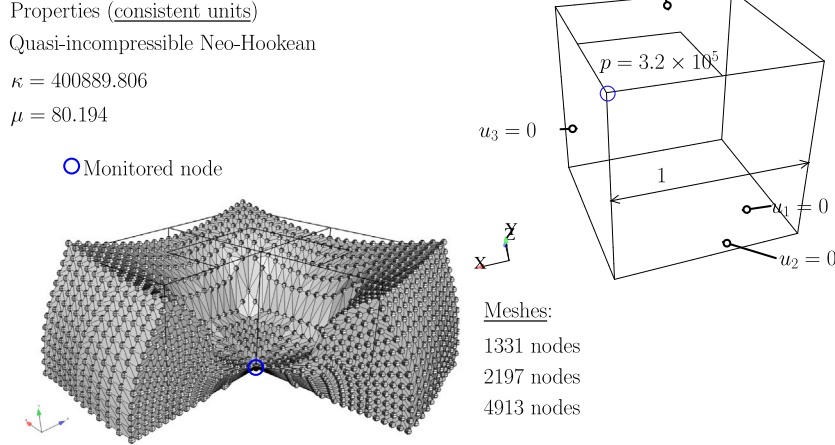1331 nodes

2197 nodes

4913 nodes

Fig. 5. Quasi-incompressible Neo-Hookean compression test.

constitutive system for $\Delta\gamma > 0$ consists of the following equations:

$$\underbrace{\left[\Delta\hat{\boldsymbol{Q}}\left(\boldsymbol{C}_e^{n+1}, \Delta\gamma\right)\right]^T \cdot \boldsymbol{C}_e^{n+1} \cdot \left[\Delta\hat{\boldsymbol{Q}}\left(\boldsymbol{C}_e^{n+1}, \Delta\gamma\right)\right] - \hat{\boldsymbol{C}}_e^{\star}\left(\boldsymbol{C}^{n+1}\right)}_{\boldsymbol{r}_c\left(\boldsymbol{C}_e^{n+1}, \Delta\gamma, \boldsymbol{C}^{n+1}\right)} = \boldsymbol{0} \tag{54}$$

$$\phi_\star \left[\boldsymbol{C}^{n+1} \cdot \hat{\boldsymbol{S}}_e\left(\boldsymbol{C}^{n+1}\right)\right] = 0 \tag{55}$$

Since $\boldsymbol{C}_e^{n+1}$ is symmetric, Voigt notation can be used, $\mathbf{C}_e^{n+1} = \text{Voigt}\left[\boldsymbol{C}_e^{n+1}\right]$ and $\mathbf{r}_c\left(\boldsymbol{C}_e^{n+1}, \Delta\gamma, \mathbf{C}^{n+1}\right) = \text{Voigt}\left[\boldsymbol{r}_c\left(\boldsymbol{C}_e^{n+1}, \Delta\gamma, \boldsymbol{C}^{n+1}\right)\right]$. Omitting the function arguments for conciseness, the Newton–Raphson iteration for $\mathbf{C}_e^{n+1}$ (Voigt form) and $\Delta\gamma$ is written as:

$$\underbrace{\begin{bmatrix} \dfrac{\partial \mathbf{r}_c}{\partial \mathbf{C}_e^{n+1}} & \dfrac{\partial \mathbf{r}_c}{\partial \Delta\gamma} \\ \dfrac{\partial \phi}{\partial \mathbf{C}_e^{n+1}} & 0 \end{bmatrix}}_{\boldsymbol{J}} \underbrace{\left\{ \begin{array}{c} \Delta\mathbf{C}_e^{n+1} \\ \Delta\Delta\gamma \end{array} \right\}}_{\Delta\mathbf{Y}} = -\underbrace{\left\{ \begin{array}{c} \mathbf{r}_c\left(\mathbf{C}_e^{n+1}, \Delta\gamma, \mathbf{C}^{n+1}\right) \\ \phi_\star\left[\mathbf{C}_e^{n+1} \cdot \hat{\mathbf{S}}_e\left(\mathbf{C}_e^{n+1}\right)\right] \end{array} \right\}}_{\mathbf{r}} \tag{56}$$

with $\mathbf{Y} = \left\{ \mathbf{C}_e^{n+1} \quad \Delta\gamma \right\}^T$ being the constitutive unknowns for this problem. Following $\mathbf{C}_e^{n+1}$, $\boldsymbol{Q}_p^{n+1}$ is determined by (52) and the second Piola–Kirchhoff stress at step $n+1$ is given in tensor notation by:

$$\check{\boldsymbol{S}}^{n+1}\left(\underbrace{\boldsymbol{C}_e^{n+1}, \Delta\gamma}_{\mathbf{Y}}\right) = \boldsymbol{Q}_p^n \cdot \left[\Delta\hat{\boldsymbol{Q}}\left(\mathbf{C}_e^{n+1}, \Delta\gamma\right)\right]^{-1} \cdot \hat{\boldsymbol{S}}_e\left(\mathbf{C}_e^{n+1}\right)$$
$$\cdot \left\{ \left[\Delta\hat{\boldsymbol{Q}}\left(\mathbf{C}_e^{n+1}, \Delta\gamma\right)\right]^{-1} \right\}^T \cdot \left(\boldsymbol{Q}_p^n\right)^T \tag{57}$$

Stress sensitivity, the determination of the consistent modulus, with $\mathbf{S}^{n+1} = \text{Voigt}\left[\boldsymbol{S}^{n+1}\right]$, is determined as follows:

$$\frac{d\mathbf{S}^{n+1}}{d\mathbf{C}^{n+1}} = \frac{\partial\hat{\mathbf{S}}^{n+1}}{\partial\mathbf{C}_e^{n+1}} \cdot \frac{d\mathbf{C}_e^{n+1}}{d\mathbf{C}^{n+1}} + \frac{\partial\hat{\mathbf{S}}^{n+1}}{\partial\Delta\gamma} \frac{d\Delta\gamma}{d\mathbf{C}^{n+1}} \tag{58}$$

In (58), a single product dot $\cdot$ is adopted for double contraction of quantities in Voigt form. From (58) we can conclude that $\mathscr{C}$ is determined as a function of the solution of (56), since

$$d\mathbf{Y}/d\mathbf{C}^{n+1} = -\boldsymbol{J}^{-1} \cdot \partial\mathbf{r}/\partial\mathbf{C}^{n+1} \tag{59}$$

therefore, stress sensitivity is simply given by:

$$\frac{d\mathbf{S}^{n+1}}{d\mathbf{C}^{n+1}} = -\left(d\hat{\mathbf{S}}^{n+1}/d\mathbf{Y}\right) \cdot \left(d\mathbf{Y}/d\mathbf{C}^{n+1}\right) \tag{60}$$

When hardening is present, the effective plastic strain rate follows the integration of (51):

$$\varepsilon_p^{n+1} = \varepsilon_p^n + \Delta\gamma \frac{\boldsymbol{T}_e : \boldsymbol{N}(\boldsymbol{T}_e)}{\sigma_y} \tag{61}$$

4.3. Specific yield function

The nondimensional yield function is given by:

$$\phi_\star\left(\boldsymbol{T}_e\right) = \frac{\sigma_{\text{eq}}\left(\boldsymbol{T}_e\right)}{\sigma_y} - 1 \tag{62}$$

where, as a prototype equivalent stress, a specific Hill48 criterion (1948 [35]) is adopted. The general form of the Hill48 equivalent stress σ_{eq} is written as:

$$\sigma_{\text{eq}}\left(\boldsymbol{T}_e\right)$$
$$= \sqrt{F\left(T_{22} - T_{33}\right)^2 + G\left(T_{33} - T_{11}\right)^2 + H\left(T_{11} - T_{22}\right)^2 + 2S_1\left(T_4^s\right)^2 + 2S_2\left(T_5^s\right)^2 + 2S_3\left(T_6^s\right)^2} \tag{63}$$

where the subscript e of $\boldsymbol{T}_e$ is omitted for conciseness). In (63), the superscript s is adopted to indicate a symmetrized quantity. For example, $T_6^s = \frac{1}{2}\left(T_{23} + T_{32}\right)$. Introducing the yield ratios, $y_1, \ldots, y_6$ as constitutive data, we have for F, G, H, $S_{1,\ldots,3}$:

$$F = \frac{1}{2}\left(\frac{1}{y_2^2} + \frac{1}{y_3^2} - \frac{1}{y_1^2}\right) \tag{64}$$
$$G = \frac{1}{2}\left(\frac{1}{y_1^2} + \frac{1}{y_3^2} - \frac{1}{y_2^2}\right)$$
$$H = \frac{1}{2}\left(\frac{1}{y_1^2} + \frac{1}{y_2^2} - \frac{1}{y_3^2}\right)$$
$$S_k = \frac{3}{2}\left(y_{k+3}^2\right) \quad k = 3, \ldots, 6$$

We note that many other yield criteria can be used, since any specific form of $\sigma_{\text{eq}}\left(\boldsymbol{T}_e\right)$ can be inserted. Specific yield criteria for hexagonal closed-packed crystalline structures, such as Cazacu and Barlat [36] can be directly applied. Along those lines, the work of Chen et al. regarding tension/compression asymmetry performs a comparison between these yield criteria [37].

5. Numerical tests

Numerical tests were performed with the code from the leading Author, SimPlas [39], and the specific source code for EFG was created using Mathematica [40] with the AceGen add-on [16,41]. Source code for the equations in this work is available via Github [42].

5.1. Thick cylinder under pressure

We now consider a thick cylinder (internal radius a and external radius b) under internal pressure p, as discussed in chapter 6 of
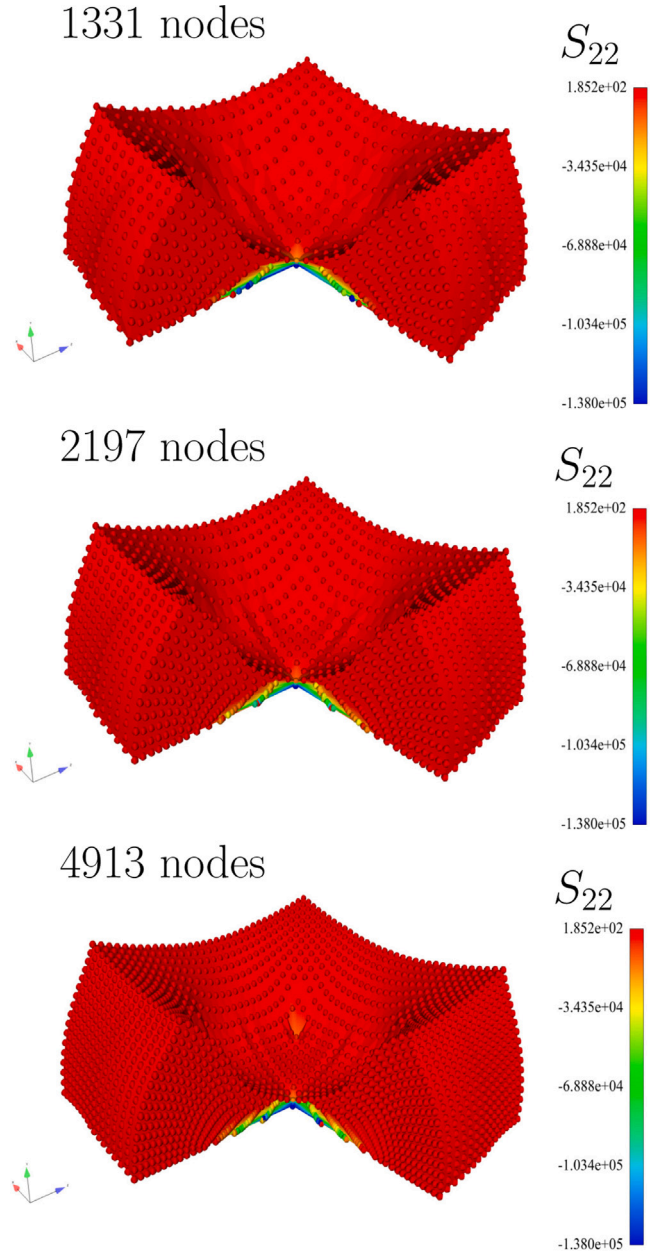
1331 nodes

S_{22}

1.852e+02

-3.435e+04

-6.888e+04

-1.034e+05

-1.380e+05

2197 nodes

S_{22}

1.852e+02

-3.435e+04

-6.888e+04

-1.034e+05

-1.380e+05

4913 nodes

S_{22}

1.852e+02

-3.435e+04

-6.888e+04

-1.034e+05

-1.380e+05

Fig. 6. Quasi-incompressible Neo-Hookean compression test, S_{22} contour plots, comparison of node densities. $n = 30$ with quadratic basis.

(a) $n = 15$, linear basis ($m = 4$), effect of mesh density for linear basis

(b) $n = 20$, quadratic basis ($m = 10$), effect of mesh for quadratic basis

(c) 2197 nodes, quadratic basis ($m = 10$), effect of support n

Fig. 7. Quasi-incompressible Neo-Hookean compression test. Finite element results from a stabilized mixed formulation by Caylak and Mahnken [34] are also presented.

Chakrabarty [33]. Internal pressure Onset of yielding is obtained, in the plane strain case is given by:

$$p_e = \sigma_y \frac{(b^2 - a^2)}{b^2 \sqrt{\frac{a^4(1-2\nu)^2 + 3b^4}{b^4}}} \tag{65}$$

where ν is the Poisson coefficient. Using the condition $p < \sigma_y 2\sqrt{3}(1-\nu)/(6\nu-3)$, a solution is possible using a correction of Tresca criterion. For the non-hardening case, we have the following stress components:

$$\sigma_r = \frac{\sigma_y}{\sqrt{3}} \begin{cases} \left(\frac{c^2}{b^2} - \ln\frac{c^2}{r^2} - 1\right) & c > r \geq a \\ \left(1 - \frac{b^2}{r^2}\right)\frac{c^2}{b^2} & b \geq r \geq c \end{cases} \tag{66}$$

$$\sigma_\theta = \frac{\sigma_y}{\sqrt{3}} \begin{cases} \left(\frac{c^2}{b^2} - \ln\frac{c^2}{r^2} + 1\right) & c > r \geq a \\ \left(1 + \frac{b^2}{r^2}\right)\frac{c^2}{b^2} & b \geq r \geq c \end{cases} \tag{67}$$

Pressure is related to the radius coordinate of the elasto-plastic interface c as:

$$p(c) = \frac{\sigma_y}{\sqrt{3}}\left(1 - \frac{c^2}{b^2} + 2\ln\frac{c}{a}\right) \tag{68}$$

from which, the fully-plastic condition is obtained for $p(b) = \left(2\sigma_y/\sqrt{3}\right)\ln b/a$. For $b = 2a$, $p(b) \cong 0.800377\sigma_y$. Fig. 2 shows the results for $a = 1$, $b = 2$, $\nu = 0.3$ and $E = 1$ using a quadratic basis. Stress contour plots are very smooth, as shown in Fig. 2. Comparing the results with the
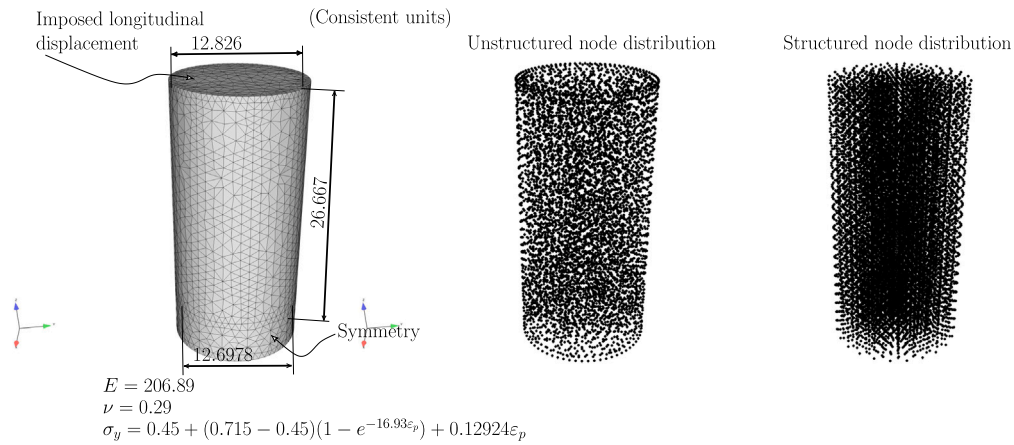
Fig. 8. Relevant dimensions and mesh for the Neo-Hookean/Hill48 tension test.
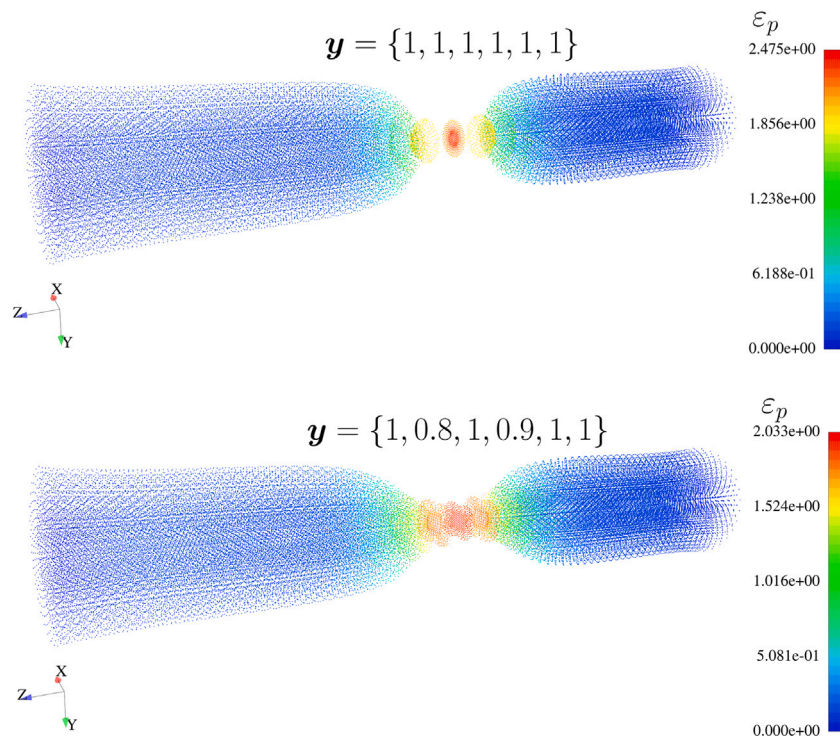

Fig. 9. Tension test: deformed configurations for both yield functions with the corresponding effective plastic strain colors. (For interpretation of the references to colour in this figure legend, the reader is referred to the web version of this article.)

closed-form solutions in Chakrabarty and with a crossed-configuration FE triangular mesh, we can observe the great advantage of this EFG formulation in Fig. 3 where $n = 10$ was adopted for EFG. Comparing $n = 10$ and $n = 20$, see Fig. 4, we conclude that higher stress accuracy is obtained for $n = 20$, although at an added computational cost.

To assess the effect of the support on the stress error, we compare $n = 10$ with $n = 20$ in Figure...

5.2. Block compression

Using a quasi-incompressible hyperelastic law, we test the present finite-strain EFG formulation with a benchmark consisting of an asymmetric compression of a block described by Reese, Wriggers and Reddy [43]. The strain–energy density function adopted here is the following:

$$\Psi = \frac{1}{2}\mu \left(\text{tr} \left[\hat{C} \right] - 3 \right) + \frac{1}{2}\kappa \left(\log \left[J \right] \right)^2 \tag{69}$$

In (69), $\hat{C} = J^{-2/3}C$ and $C = F^T F$ with $\kappa = 400\,889.806$ and $\mu = 80.194$ (consistent units). In this example, large compressive strains and strain gradients are combined. It is a demanding test to assess the effect of the polynomial basis and support size. The relevant data for the compression test is shown in Fig. 5. Due to the presence of two symmetry planes, only one quarter of the geometry is discretized. Relevant properties and dimensions for this problem are shown in Fig. 5. We also show the deformed configuration including the support tetrahedra. Three different nodal distributions are employed, with 1331, 2197 and 4913 nodes. In Fig. 6 the effect of mesh density in the deformed configuration is shown. In the three cases, very large deformations are reached and no indication of instabilities was apparent. The stress S_{22} contour plot is smooth, even in the highly deformed region, confirming the effectiveness of the EFG formulation.

In Fig. 7 results for $n = 15$ with $m = 4$, $n = 20$ with $m = 4$ and $n = 10, 20$ and 30 with $m = 10$ are shown. For comparison, we also report
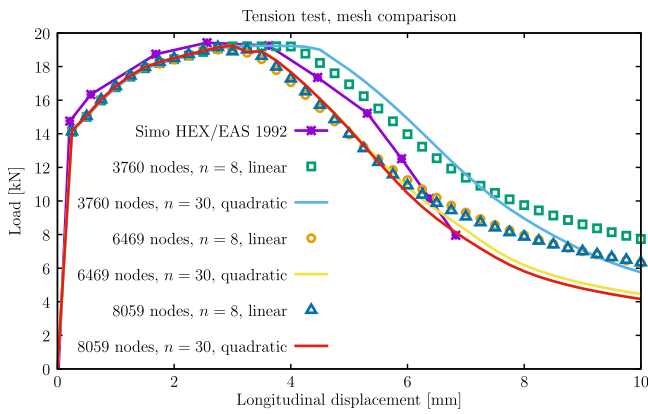
(a) Comparison with EAS hexahedral elements ([44, 43]).
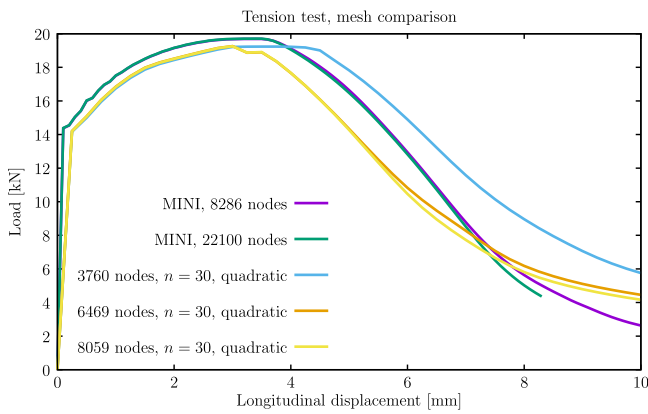
(b) Comparison with mixed tetrahedral elements ([45]).

Fig. 10. Comparison with advanced finite element technology and effect of mesh density on the results with the quadratic basis. Structured mesh.

(a) Structured node case (3760 nodes): Effect of support and polynomial basis.

(b) Unstructured node case: Effect of the number of substeps n_s. 40 loading steps are adopted.

Fig. 11. Effect of structured/unstructured node distribution.

the results by Caylak and Mahnken [34], using the reduced integration hexahedron Q1R and 8 elements per edge, and a classical tetrahedron $T4$ with a crossed-configuration (i.e. a hexahedral mesh with a regular division in 24 tetrahedra). As can be observed, results with lower values of n converge to the Caylak and Mahnken solution, even in the coarser case. Finer nodal distributions produce more flexible results and with the quadratic basis ($m = 10$) with $n = 20$ results are nearly insensitive to the nodal refinement. We also conclude that with a strictly sufficient support, i.e. $n = 10$ for $m = 10$, exceedingly flexible results are obtained.

5.3. Tension test

We apply the EFG discretization algorithm to the tension test originally discussed by Simo and co-workers in the context of J_2 plasticity [7] (see also the 1993 Ref. [44] where the test is explored in detail). Geometry, boundary conditions and material properties are summarized in Fig. 8, along with the two cases of nodal distribution: structured and unstructured, as this was found to have an effect on the results. contour plot of the effective plastic strain, given by Eq. (61). The specific yield stress σ_y is given by the hardening law shown in Fig. 8. Fig. 9 shows the deformed configurations resulting from both yield functions.

Comparatively to mixed FE formulations, results are competitive but slightly distinct in behavior. When compared with enhanced assumed strain hexahedra, for example Simo and Armero [45], the post-localization behavior is distinct, see Fig. 10(a). We note that two significant differences exist: (i) Simo and Armero adopted a formulation based on the Kirchhoff stress tensor and radial-return mapping for J_2 plasticity and (ii) hexahedra tend to reproduce the incompressibility condition with sharper stretching. A comparison with mixed tetrahedra,
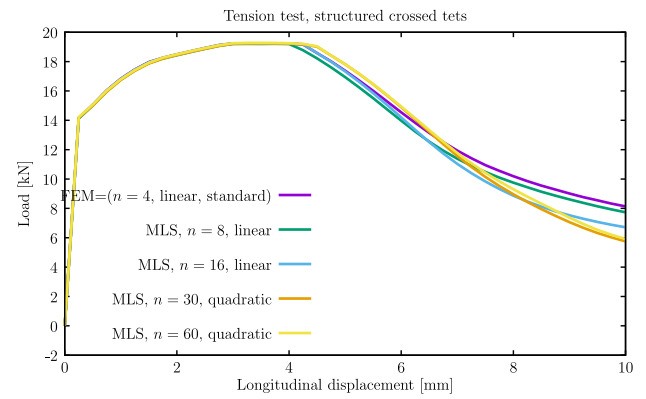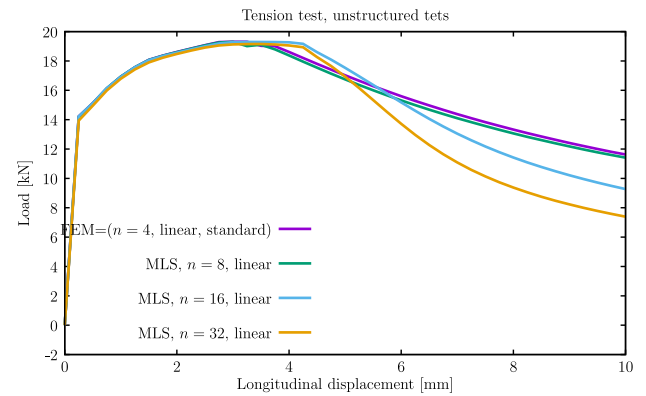
specifically the MINI element by Arnold, Brezzi and Fortin [46] is shown in Fig. 10(b). Our own implementation of MINI element was adopted, with the same constitutive integrator.

For the structured mesh with 3760 nodes, the effect of n and m (linear basis has $m = 4$ and quadratic basis $m = 10$), Fig. 11(a) shows the results. These are clear: a quadratic basis accentuates the post-localization necking behavior and, for the same basis, higher n produces sharper results.

When adopting an unstructured node distribution, a less pronounced post-localization behavior is exhibited, see Fig. 11(b), which shows the important effect of using a quadratic basis in this case.

5.4. Upsetting test

We resort to M. Puso's upsetting test [38] in its two elasto-plastic versions (linear and power hardening). Geometry, boundary conditions and constitutive properties for this test are shown in Fig. 12. Three uniform meshes are adopted for comparison, containing 236, 527 and 903 nodes. Nodes are forced to remain above an horizontal plane by a non-penetration condition using Lagrange multipliers. The elasto-plastic case described by M. Puso is the most demanding and it is reported that only their nodally integrated and stabilized UT4s provides acceptable results from the stability and accuracy standpoints. We point out that, in [38], a stabilization *parameter* is required. In the present formulation, no parameters are required and no hourglass instabilities were detected. Fig. 13 shows the very smooth contour plots for ε_p and hydrostatic σ_H. Fig. 14(a) presents a comparison between nodal distributions, support sizes (n) and basis dimension. All three factors contribute to a more flexible behavior: finer meshes are less stiff, larger supports produce softer behavior and quadratic basis produce results beneath the reaction–displacement curve reported in [38].

Properties (**consistent units**):

$E = 29870$

$\nu = 0.3$

$\sigma_y = 41 + 205\overline{\varepsilon}_p$ (linear hardening)

$\sigma_y = 112(\overline{\varepsilon}_p + 0.0113)^{0.227}$ (power law)

Nodes:

527 nodes
903 nodes

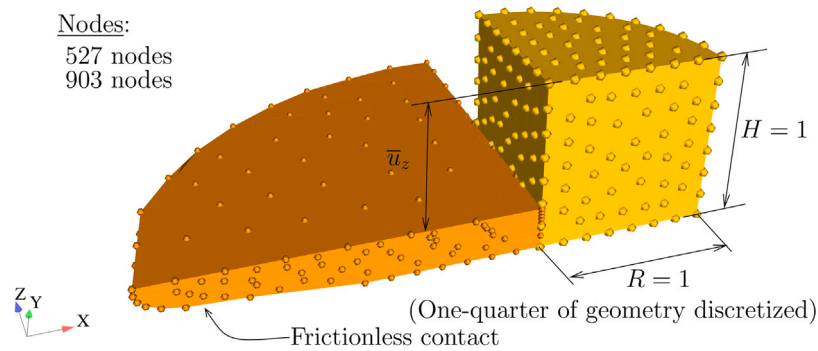**Fig. 12.** Upsetting test: relevant data.

Linear hardening case

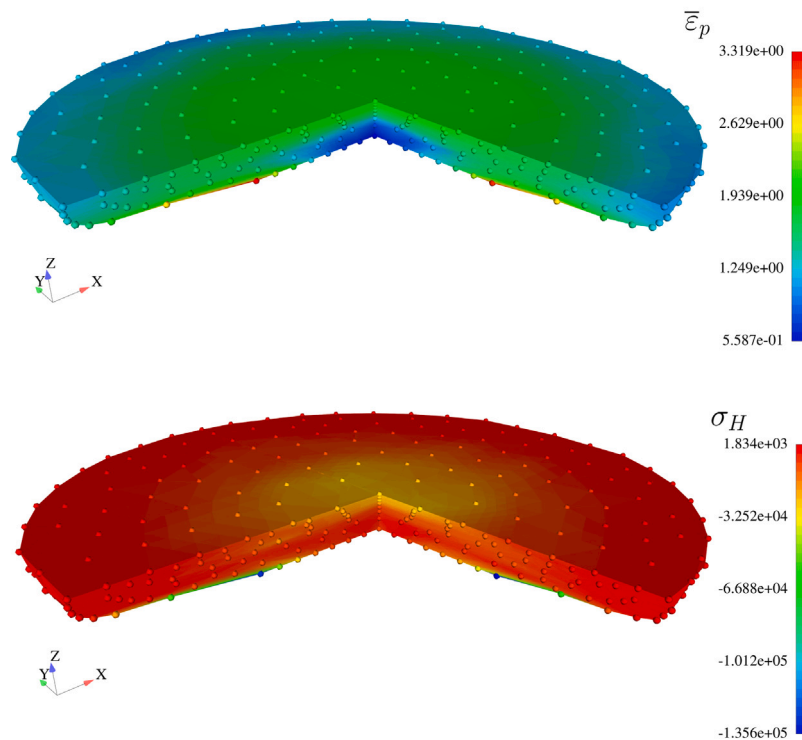**Fig. 13.** Upsetting test: contour plots (ε_p, $\sigma_H = {}^{\mathrm{tr}[S]}/_3$) for the linear hardening case.

6. Conclusions

We introduced a tetrahedra-based least-squares EFG which incorporates the following properties:

- An initial perturbation of internal FE nodal positions is performed for efficiency reasons (low n).
- Linear and quadratic shape functions and Lagrangian diffuse derivatives are defined ab-initio for the entire analysis.
- A pre-established nodal support is imposed, where all nodes of the corresponding tetrahedron are forced to be present.

- A tetrahedra integration with single point quadrature is adopted.
- Constitutive integration makes use of the Mandel stress tensor and iteration on $\boldsymbol{C}_e$ [15].

Implementation is straightforward and was performed in SimPlas [39] with AceGen [41] and Mathematica [40]. Four benchmark tests were performed, which allow the following conclusions:

- Even with small values of n, results are highly competitive with established finite elements.
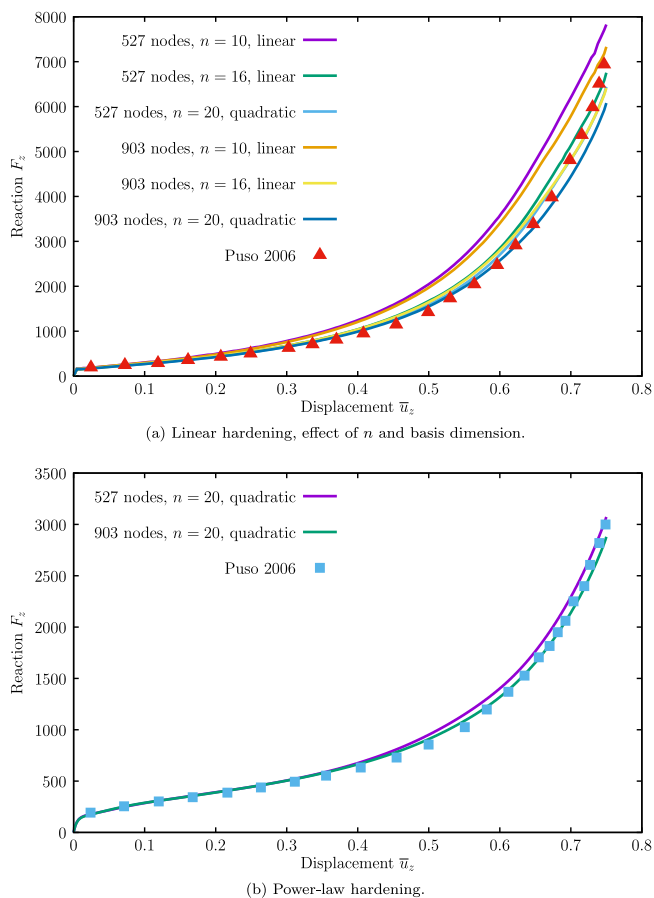- Results with coarse point distributions exhibit a large dependence on the number of support points n.

(a) Linear hardening, effect of n and basis dimension.

(b) Power-law hardening.

Fig. 14. Displacement/reaction for the upsetting test. Effect of n, m and comparison with results reported by M. Puso [38].

- Stress quality measured as the distance to the closed-form solution in the pressurized cylinder problem was found to be superior to classical FEM solutions.
- A finite strain solution is simpler than with mixed finite elements and on-par with displacement-based FEM.

Developments into strain localization and fracture fit into this framework, since stress quality is of paramount importance in modeling real materials.

Acknowledgments

References

[1] Lee NS, Bathe KJ. Effects of element distortions on the performance of isoparametric elements. Internat J Numer Methods Engrg 1993;36:3553–76.

[2] Peng X, Atroshchenko E, Kerfriden P, Bordas SPA. Isogeometric boundary element methods for three dimensional static fracture and fatigue crack growth. Comput Methods Appl Math 2017;316:151–85.

[3] Bathe K-J. Finite element procedures. Prentice-Hall; 1996.

[4] Belytschko T, Lu YY, Gu L. Element-free Galerkin methods. Internat J Numer Methods Engrg 1994;37:229–56.

[5] Lancaster P, Salkauskas K. Surfaces generated by moving least squares methods. Math Comput 1981;37(155):141–58.

[6] Rabczuk T, Belytschko T, Xiao SP. Stable particle methods based on Lagrangian kernels. Comput Methods Appl Math 2004;193:1035–63.

[7] Simo JC. Algorithms for static and dynamic multiplicative plasticity that preserve the classical return mapping schemes of the infinitesimal theory. Comput Methods Appl Math 1992;99:61–112.

[8] Simo JC, Hughes TJR. Computational inelasticity. corrected second printing ed.. Springer; 2000.

[9] Rossi R, Alves MK. On the analysis of an EFG method under large deformations and volumetric locking. Comput Mech 2007;39:381–99.

[10] Chen J-S, Hillman M, Chi S-W. Meshfree methods: Progress made after 20 years. J Eng Mech ASCE 2017;143(4):04017001.

[11] Cai Y, Zhuang X, Augarde C. A new partition of unity finite element free from the linear dependence problem and possessing the delta property. Comput Methods Appl Math 2010;199:1036–43.

[12] Boroomand B, Parand S. Towards a general interpolation scheme. Comput Methods Appl Math 2021;381:113830.

[13] Yu SY, Peng MJ, Cheng H, Cheng YM. The improved element-free Galerkin for three-dimensional elastoplasticity problems. Eng Anal Bound Elem 2019;104:215–24.

[14] Bourantas G, Zwick BF, Joldes GR, Wittek A, Miller K. Simple and robust element-free Galerkin method with almost interpolating shape functions for finite deformation elasticity. Appl Math Model 2021;96:284–303.

[15] Areias P, Rabczuk T, Ambrósio J. Extrapolation and c_e-based implicit integration of anisotropic constitutive behavior. Internat J Numer Methods Engrg 2021;122:1218–40.

[16] Wriggers P. Nonlinear finite element methods. Springer; 2008.

[17] Huerta A, Méndez SF. Locking in the incompressible limit for the element-free Galerin method. Internat J Numer Methods Engrg 2001;51:1361–83.

[18] Most T, Bucher C. A moving least squares weighting function for the element-free Galerkin method which almost fulfills essential boundary conditions. Struct Eng Mech 2005;21(3):315–32.

[19] Most T, Bucher C. New concepts for moving least squares: An interpolation non-singular weighting function and weighted nodal least squares. Eng Anal Bound Elem 2008;32:461–70.

[20] Belytschko T, Krongauz Y, Organ D, Fleming M, Krysl P. Meshless methods: an overview and recent developments. Comput Methods Appl Math 1996;139:3–47.

[21] Golub GJ, Van Loan CF. Matrix computations. 3d ed.. Johns Hopkins; 1996.

[22] Dehghan M, Abbaszadeh M. Interpolating stabilized moving least squares (MLS) approximation for 2D elliptic interface problems. Comput Methods Appl Math 2018;328:775–803.

[23] Belytschko T, Liu WK, Moran B. Nonlinear finite elements for continua and structures. John Wiley & Sons; 2000.

[24] Areias P, César de Sá JMA, Conceição António CA, Fernandes AA. Analysis of 3D problems using a new enhanced strain hexahedral element. Internat J Numer Methods Engrg 2003;58:1637–82.

[25] Areias P, Tiago C, Carrilho Lopes J, Carapau F, Correia P. A finite strain raviart-thomas tetrahedron. Eur J Mech A Solids 2020;80:103911.

[26] Mandel J. Equations constitutives et directeurs dans les milieux plastiques et viscoplastiques. Int J Solids Struct 1973;9:725–40.

[27] Eidel B, Gruttmann F. Elastoplastic orthotropy at finite strains: multiplicative formulation and numerical implementation. Comput Mater Sci 2003;28:732–42.

[28] Kröner E. Allgemeine kontinuumstheorie der versetzungen und eigenspannungen. Arch Ration Mech Anal 1960;4:273–334.

[29] Lee EH. Elasto-plastic deformation at finite strains. J Appl Mech ASME 1969;36:1–6.

[30] Lubliner J. Plasticity theory. Macmillan; 1990.

[31] Gurtin ME. An introduction to continuum mechanics. Mathematics in science and engineering, vol. 158, 111 Fifth Avenue, New York, New York 10003: Academic Press; 1981.

[32] Mandel J. Foundations of continuum thermodynamics. London: MacMillan; 1974, p. 283–304, chapter Thermodynamics and Plasticity.

[33] Chakrabarty J. Theory of plasticity. 3rd ed.. Oxford, UK: Butterworth-Heinemann; 2006.

[34] Caylak I, Mahnken R. Stabilization of mixed tetrahedral elements at large deformations. Internat J Numer Methods Engrg 2012;90:218–42.

[35] Hill R. A theory of yielding and plastic flow of anisotropic metals. Proc R Soc Lond 1948;193:281–97.

[36] Cazacu O, Barlat F. A criterion for description of anisotropy and yield differential effects in pressure-insensitive metals. Int J Plast 2004;20:2027–45.

[37] Chen L, Zhang J, Zhang H. Anisotropic yield criterion for metals exhibiting tension-compression asymmetry. Adv Appl Math Mech 2021;13:701–23.

[38] Puso MA, Solberg J. A stabilized nodally integrated tetrahedral. Internat J Numer Methods Engrg 2006;67:841–67.

[39] Areias P. Simplas. http://www.simplassoftware.com. Portuguese Software Association (ASSOFT) registry number 2281/D/17.

[40] Wolfram Research Inc. Mathematica. 2007.

[41] Korelc J. Multi-language and multi-environment generation of nonlinear finite element codes. Eng Comput 2002;18(4):312–27.

[42] Areias P. EFG MLS. 2021, https://github.com/PedroAreiasIST/EFG.

[43] Reese S, Wriggers P, Reddy BD. A new locking-free brick element technique for large deformation problems in elasticity. Comput Struct 2000;75:291–304.

[44] Simo JC, Armero F, Taylor RL. Improved versions of assumed strain tri-linear elements for 3D finite deformation problems. Comput Methods Appl Math 1993;110:359–86.

[45] Simo JC, Armero F. Geometrically non-linear enhanced strain mixed methods and the method of incompatible modes. Internat J Numer Methods Engrg 1992;33:1413–49.

[46] Arnold DN, Brezzi F, Fortin M. A stable finite element for the Stokes equations. Calcolo 1984;XXI(IV):337–44.